Title: Computationally-assisted Identification of Functional Inorganic Materials

Authors: Matthew S. Dyer[1], Christopher Collins[1], Darren Hodgeman[1], Philip A. Chater[1], Antoine Demont[1], Simon Romani[2], Ruth Sayers[1], Michael F. Thomas[3], John B. Claridge[1], George R. Darling[1], and Matthew J. Rosseinsky[1]*.

Affiliations:

[1]Department of Chemistry, University of Liverpool, Crown Street, Liverpool L69 7ZD, United Kingdom

[2]Centre for Materials and Structures, School of Engineering, The Quadrangle, University of Liverpool, Brownlow Hill, Liverpool L69 3GH, United Kingdom

[3]Department of Physics, University of Liverpool, Liverpool L69 7ZE, United Kingdom

*Correspondence to: m.j.rosseinsky@liverpool.ac.uk.

Abstract:

The design of complex inorganic materials is a challenge because of the diversity of their potential structures. We present a method for the computational identification of materials containing multiple atom types in multiple geometries by ranking candidate structures assembled from extended modules containing chemically realistic atomic environments. Many existing functional materials can be described in this way, and their properties are often determined by the chemistry and electronic structure of their constituent modules. To demonstrate the approach, the oxide $Y_{2.24}Ba_{2.28}Ca_{3.48}Fe_{7.44}Cu_{0.56}O_{21}$, with a largest unit cell dimension of over 60 Å and 148 atoms in the unit cell, was isolated using a combination of this method and experimental

work, and is shown to have the properties necessary to function as a solid oxide fuel cell cathode.

Main Text:

The identification and synthesis of functional materials is a significant challenge for both experiment and theory, especially for complex crystalline materials (those containing many atoms of different elements in distinct geometries). There are a vast number of arrangements of the atoms in the unit cell of a complex structure that need to be adequately sampled for structural identification and prediction (*1*). Different theoretical approaches to this problem have been developed; some involve an unbiased search through the different atomic arrangements (*2-7*), others use existing chemical knowledge and understanding to reduce the number of arrangements considered (*8-14*).

In describing complex solid state structures it is customary to break them down in terms of modules or fragments and their combinations (*15*). Structural units such as blocks, rods or layers (as shown in Figure 1A and B for two different structural families) derived from archetypal structures are combined by structure building operators. Within this approach the combination of two or more layers from different crystal structures, a concept known as polysomatism (*16*), has proved powerful. The diverse families described as polysomatic series in terms of layers include heterogeneous structural series of intermetallics (*17*), light element networks such as the aluminium carbonitrides (*18*) (Fig. 1A), mineral families (*19*) such as the sapphirenes (*20*) and biopyriboles (*16*), and accretional series within the perovskite family (*21*) including Aurivillius and Dion-Jacobson phases, and families of hexagonal perovskites (*22*). It is possible to envisage polysomatic series using larger layers including the complex ferrites (Fig. 1B), some of the largest volume functional inorganic structures known (*23*). The functional behavior can be directly controlled by the constituent layers *e.g.* lone-pair based fluorite-like layers in the Aurivillius series can produce high

temperature ferroelectricity while the Ba-containing R and T blocks in the hexaferrites (red and blue respectively in Figure 1B) impose large magnetic anisotropy (*24*).

We use the combination of layers in the Extended Module Materials Assembly (EMMA) approach adopted here to identify new candidate structures, as outlined in Fig. 1C. First a set of extended layers (modules) must be chosen. Next the number of times each module appears within a single repeated unit cell is selected. At this point all possible permutations of the modules within the unit cell are created using chosen structure building operators; the present examples use translation along the long axis and inversion symmetry, however other symmetry operations could be included. The number of candidate structures is reduced by removing duplicates of the same cyclical stacking sequence. Those remaining are ranked according to some suitable selection criteria to give the most promising candidates for experimental synthesis. We initially ranked a large number of structures using energies obtained from a preliminary structural relaxation by classical force-field methods (*25*) (though any cost function suitable for the system under study could be used). The relative stabilities of the best candidates were evaluated quantitatively using ab initio calculations (*25*). The extended modules encode bonding information directly into the candidate structures, mainly creating structures where atoms are in chemically sensible environments where the use of force-fields is valid. There is no conceptual limit to the nature or size of the modules, although we have concentrated on one atom thick metal oxide layers in this study. A practical limit exists on the number of modules within a single repeat, since the total number of permutations becomes very large with more than 15-20 modules. This limitation could be circumvented by searching through possible permutations using methods such as evolutionary algorithms (*5, 7*). Finite computational resources will also limit the overall size of the generated unit cell (a product of the number of modules, and their individual sizes).

The perovskite ABO_3 structure can be described by stacking AO rock salt and BO_2 square layer modules containing large A and smaller transition metal B cations. There are a large number of possible superstructures derived by coupled cation site and anion vacancy ordering such as $YBa_2Ca_2Fe_5O_{13}$, which functions as a solid oxide fuel cell (SOFC) cathode (26). We select anion-vacancy containing modules to construct superstructures containing Fe^{3+} ions. Such units afford both electronic conductivity and oxide ion transport, which are required for functionality as an SOFC cathode. We validated the EMMA approach by reproducing the structure of this material. By generating a set of structures using $2Y_4 + 4Ba_4O_4 + 4Ca_4O_4 + 2Fe_4O_4 + 8Fe_4O_8$ modules (Fig. 2A) in a cell of dimensions $2a_p \times 2a_p \times 10a_p$, where $a_p \approx 3.9$ Å is the dimension of an ABO_3 unit cell, we obtain 14,190 structures with 184 atoms per unit cell. The $AO_{1-\delta}$ and $BO_{2-\delta}$ modules were permuted separately. For each permuted arrangement of $AO_{1-\delta}$ and $BO_{2-\delta}$ modules, a candidate structure was constructed by stacking alternate $AO_{1-\delta}$ and $BO_{2-\delta}$ modules. During the initial relaxation (25) 7,628 structures failed to converge due to poor starting geometries and were rejected. The three structures shown in Fig. 2C are significantly lower in energy than the others (Fig. 2B), with an energetic spread of only 0.02 eV/ Formula Unit (FU, here $YBa_2Ca_2Fe_5O_{13}$), and a separation in energy of 0.15 eV/FU to the next structure; the experimental $YBa_2Ca_2Fe_5O_{13}$ structure is the second most stable. These four most stable structures were then relaxed using DFT (25) to improve the energetics. The most stable structure by 0.09 eV/FU using DFT (Fig. 2D) corresponds to the known experimental structure for $YBa_2Ca_2Fe_5O_{13}$, demonstrating that the EMMA approach can correctly identify a known structure.

We experimentally explored the partial substitution of 7% Cu^{2+} for Fe^{3+} in order to increase the electronic conductivity of $YBa_2Ca_2Fe_5O_{13}$ and therefore improve its performance as an SOFC cathode. This resulted in a multiphasic sample, suggesting that other phases are accessible near this composition. One phase gave a powder X-ray diffraction pattern with

Bragg reflections indicative of an $8a_p$ repeat and an EDX-derived cation composition of $Y_{2.1(2)}Ba_{1.8(2)}Ca_{4.1(2)}Fe_{7.4(2)}Cu_{0.6(2)}$. We attempted to identify the structure of this phase by the EMMA method which targeted the idealised compositions $Y_2Ba_2Ca_4Fe_8O_{21}$ and $Y_2Ba_2Ca_4Fe_{7.5}Cu_{0.5}O_{21}$ (Fig. 3). These are candidate Fe^{3+}/Cu^{2+} compositions based on eightfold multiples of the basic ABO_3 perovskite formula unit with repeat dimension a_p ($8a_p$). Using these target compositions and a box of dimensions $2a_p \times 2a_p \times 8a_p$ (where $a_p = 3.9$ Å) accommodating multiple orderings of the cations based on the target composition, we generated 6,300 structures for $Y_2Ba_2Ca_4Fe_8O_{21}$ using three chemically sensible choices of modules, expanded from those used for $YBa_2Ca_2Fe_5O_{13}$ in which the constituent modules were already known. The module sets each included $2Ba_4O_4 + 4Ca_4O_4 + 5Fe_4O_8$ modules and then a combination of either $2Y_4 + Fe_4O_4 + 2Fe_4O_8$; $Y_4 + Y_4O_4 + 2Fe_4O_4 + Fe_4O_8$; or $2Y_4O_4 + 3Fe_4O_4$ modules. The three sets of modules place the oxygen vacancies in different combinations of Y_4 and Fe_4O_4 layers, allowing for flexibility in the final structures while using chemical intuition to guide the initial location of oxygen vacancies. 17,640 structures for $Y_2Ba_2Ca_4Fe_{7.5}Cu_{0.5}O_{21}$ were constructed using $2Ba_4O_4 + 4Ca_4O_4 + 2Y_4 + 5Fe_4O_8 + Fe_4O_4 + 2Fe_3CuO_8$ modules, with Cu atoms at different locations within the two Fe_3CuO_8 modules.

Following initial relaxation of the structures (Fig. 3) one $Y_2Ba_2Ca_4Fe_{7.5}Cu_{0.5}O_{21}$ structure was 0.42 eV/FU more stable than all others (Fig. 3D). We relaxed the 20 lowest energy structures at this composition using DFT, confirming that the predicted lowest energy structure is the same from both force-field and DFT calculations. The same lowest energy structure was also found for $Y_2Ba_2Ca_4Fe_8O_{21}$ (Fig 3B). We note that extensive relaxation of local structure and cell dimensions away from the initial module-constrained structures is observed at the force-field stage, suggesting that considerable movement away from the starting structures is possible, reducing the bias in the prediction due to our original choice of modules (Fig. S1). However, the lowest energy structure was only found using one of the three sets of starting

modules for $Y_2Ba_2Ca_4Fe_8O_{21}$, illustrating the need to consider a variety of different starting modules to ensure identification of the optimal final structures.

In parallel with the EMMA calculations the experimental phase diagram was investigated by synthesis at similar compositions (Fig. 4F). Synthesis of $Y_2Ba_2Ca_4Fe_{7.5}Cu_{0.5}O_{21}$ generated a polyphasic material containing a perovskite-derived phase with the apparent $8a_p$ repeat (Fig. S2). Competing phases observed in this system were two $10a_p$ phases related to $YBa_2Ca_2Fe_5O_{13}$, a $3a_p$ $Sr_2LaFe_3O_8$-related structure (27), $YCa_4Fe_5O_{13}$ and Y_2O_3. Isolation of the target compound in phase-pure form suitable for structure refinement and property characterisation requires experimental optimisation of the global composition and synthesis conditions (25) through a classical phase diagram study (Fig. 4F) to afford compound **1**, with the nominal composition $Y_{2.24}Ba_{2.28}Ca_{3.48}Fe_{7.44}Cu_{0.56}O_{21}$ (EDX-derived cation composition $Y_{2.07(15)}Ba_{2.49(20)}Ca_{3.44(5)}Fe_{7.63(18)}Cu_{0.37(7)}$). Selected area electron diffraction (SAED) (25) evaluation of this sample revealed that the longest axis in the unit cell is a $16a_p$ repeat derived from body-centring superposition of the $8a_p$ blocks (Fig. 4J and Fig. S3). A compound with the same $16a_p$ repeat, but without any Cu in the material, **2**, has been synthesised as part of a polyphasic sample at a nominal composition of $Y_{1.95}Ba_{2.1}Ca_{3.95}Fe_8O_{21}$ (Fig. S4). A second series of EMMA calculations were performed on materials with the composition $Y_2Ba_2Ca_4Fe_8O_{21}$ in the enlarged $16a_p$ repeat, adding an inversion centre to generate the body centring observed by SAED on the experimental compound to reduce the number of total permutations of modules. By using the experimental SAED results to inform the EMMA procedure, we reduced over 10^8 possible structures with $16a_p$ repeats to a restricted set of 47,040 candidate structures which have body centring in agreement with experiment (25).

The final predicted $16a_p$ structure from EMMA (Fig. 4A) contains five elements with a 61 Å longest repeat. The $16a_p$ structure consists of 9 crystallographically distinct cation sites. There are four Fe sites in three different coordination environments; one square pyramidal

6

(S_q), two octahedral (O_h) and one tetrahedral (T_d). Y cations occupy two 8 coordinate sites (between S_q Fe layers and between O_h Fe layers), while the larger Ba cations occupy a 12 coordinate site (between S_q and O_h Fe layers). Ca cations occupy two chemically similar 8 coordinate sites (between O_h and T_d Fe layers). The total B-site stacking sequence can be represented as $S_q O_h T_d O_h O_h T_d O_h S_q$. We note that the $16a_p$ structure is related to the lowest energy $8a_p$ structure found in the first set of calculations by the addition of body centring; the smaller $8a_p$ unit cell dimensions still allowed sufficient complexity for the observed local chemical environments of each ion to emerge.

The symmetrically unconstrained $16a_p$ structure from EMMA was transformed into the experimentally (SAED) determined symmetry of *Imma* (Fig. S5) and used as a starting point for Rietveld refinement with combined X-ray and neutron powder diffraction data collected on the experimentally synthesized phase **1** (Fig. 4I) (*25*). During the course of the refinement the phase composition was changed from the idealized EMMA $16a_p$ composition of $Y_2Ba_2Ca_4Fe_8O_{21}$ to that of **1**, $Y_{2.24}Ba_{2.28}Ca_{3.48}Fe_{7.44}Cu_{0.56}O_{21}$. The experimentally determined structure from Rietveld refinement closely resembles the EMMA predicted structure (Fig. 4B and 4A, respectively), with complete preservation of the predicted Fe coordination environments. The determined A-site distribution shows the same majority cation ordering as predicted by EMMA, but with significant cation mixing between layers which is both made necessary by the difference between the EMMA composition and the experimental composition and expected because of entropy considerations at the synthesis temperature. The fractional cation occupancies can be modeled by swapping the cations on the A-sites in the EMMA-derived structure and using finite temperature Monte-Carlo sampling (*25, 28*). The similarities between the predicted and refined structures are striking (Fig. 4C). The diffraction-based long-range average structure was observed in shorter length scale high-angle annular dark field scanning transmission electron microscopy (HAADF-STEM) (*25*)

imaging of **1** (Fig. 4D), which was in good agreement with a simulated HAADF-STEM image of the refined structure (Fig. 4E and Fig. S6). Mössbauer spectroscopy (*25*) also confirmed that the structure contains only Fe^{3+} in octahedral, square pyramidal and tetrahedral environments in a 2:1:1 ratio, in agreement with the calculated and refined experimental structures (Fig. S7) and iodometric titrations (*25*).

The $16a_p$ material **1** has the structural and electronic pre-requisites for mixed ionic and electronic conduction due to the presence of open-shell Fe^{3+} and anion vacancies, which was directly encoded in the choice of EMMA modules, suggesting its application as an SOFC cathode. It showed good kinetic stability, with no detectable decomposition after heating at 950°C for 5 hours. No reactivity was observed with typical electrolytes $Ce_{0.8}Sm_{0.2}O_{2-\delta}$ (SDC), $Ce_{0.9}Gd_{0.1}O_{2-\delta}$ (GDC) and $La_{0.9}Sr_{0.1}Ga_{0.8}Mg_{0.2}O_{3-\delta}$ (LSGM) at common intermediate temperature (IT)-SOFC operating and processing temperatures of 1023 K and 1223 K respectively (Fig. S8). The $16a_p$ material **1** shows an improved stability to the state-of-the-art barium-rich cathode material, $Ba_{0.5}Sr_{0.5}Co_{0.8}Fe_{0.2}O_{3-\delta}$ (BSCF), which decomposes to a hexagonal phase (*29*) and reacts with SDC (*30*) under the same conditions used in the reactivity and stability tests. Symmetrical cells were fabricated by screen printing porous cathode layers on both faces of a dense GDC electrolyte disc and the resulting area specific resistance (ASR) value of 0.27 Ω cm^2 at 973K compares well with the common IT-SOFC cathode $La_{0.6}Sr_{0.4}Co_{0.2}Fe_{0.8}O_{3-\delta}$ (LSCF, 0.46 Ω cm^2) (*31*) and the layered $10a_p$ $YBa_2Ca_2Fe_5O_{13}$ cathode (0.88 Ω cm^2) (*26*) (Fig. 4H). DC conductivity measurements are shown in Fig. S9. The EMMA method has therefore identified a structure which has experimentally demonstrated functionality as an SOFC cathode material.

Compounds **1** and **2** are likely to be metastable at temperatures below ≈1250 K, based on both experimental and computational evidence. To produce phase-pure **1** ($16a_p$) it is necessary to quench from the synthesis temperature (Fig. S10); slow cooling produces a

mixed phase sample containing a significant proportion of $10a_p$. Calculated enthalpies of reaction at 0 K based on DFT predict that $Y_2Ba_2Ca_4Fe_8O_{21}$ ($16a_p$) is less stable than a multiphase assemblage of $YFeO_3 + Ca_2Fe_2O_5 + YBa_2Ca_2Fe_5O_{13}$ ($10a_p$). Finite temperature effects must be included to explain the synthesis of **1** and **2** (supplementary online text). In a complex compositional range of this type, reaction conditions often have a controlling influence on phase stability, leading to the conclusion that a practical target is to develop computation to assist rather than to direct the synthesis of such complex phases. Nevertheless we have demonstrated the use of EMMA in searching a phase diagram to find new structures, by investigating the (Y, Ba, Ca, Fe^{3+}, O) phase diagram for layered phases with $7a_p$ long axis repeats (supplementary online text, Fig. S11).

By including an initial bias towards using specific modules, EMMA provides a compromise between exhaustive approaches, which seek to sample all of phase space, and the need to predict complex structures. It can identify candidate structures for compositionally and structurally complex inorganic materials, given a reasonable choice of starting modules. Furthermore, the large set of ranked structures generated by EMMA contains a wealth of information, which can be analysed further to gain more general understanding (supplementary online text, Fig. S12). The modular approach adopted in EMMA allows desired functional properties to be built into the predicted structures; the selection of modules containing the relevant chemical bonding known to give rise to functional behaviour in other materials allows the targeting of specific functions.
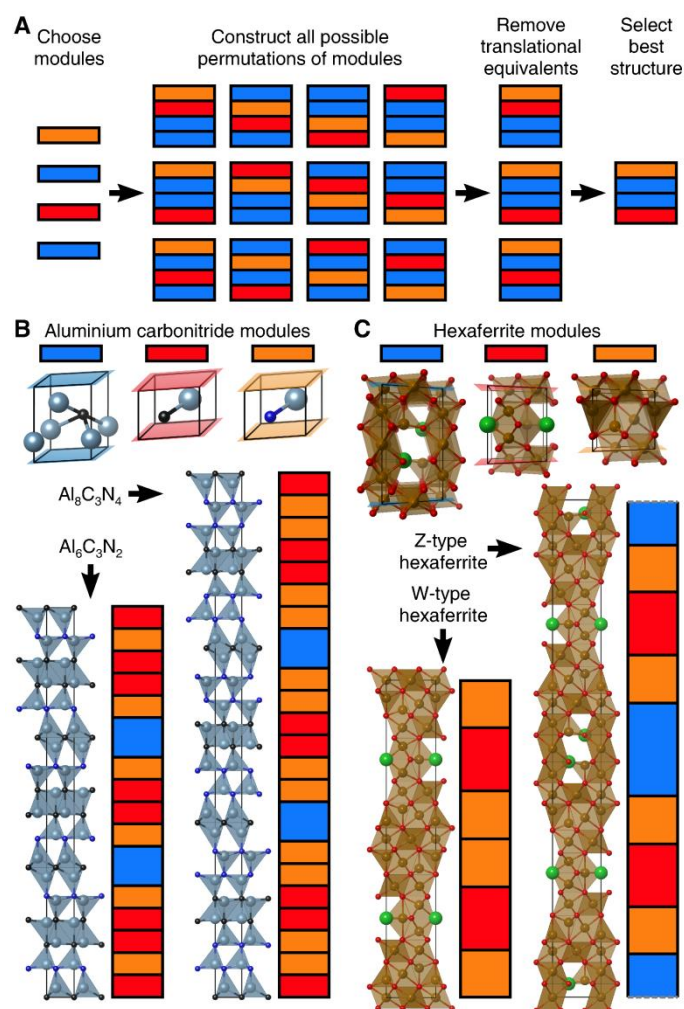
References and Notes:

1. C. W. Lehmann, Crystal structure prediction-Dawn of a new era. *Angew. Chem. Int. Ed.* **50**, 5616 (2011).
2. C. R. A. Catlow, A. N. Cormack, F. Theobald, Structure prediction of transition-metal oxides using energy-minimization techniques. *Acta Crystallogr.* **B40**, 195 (1984).
3. R. Martonak, A. Laio, M. Parrinello, Predicting crystal structures: The Parrinello-Rahman method revisited. *Phys. Rev. Lett.* **90**, 075503 (2003).

4. M. A. Neumann, F. J. J. Leusen, J. Kendrick, A major advance in crystal structure prediction. *Angew. Chem. Int. Ed.* **47**, 2427 (2008).

5. A. R. Oganov, Y. M. Ma, A. O. Lyakhov, M. Valle, C. Gatti, Evolutionary crystal structure prediction as a method for the discovery of minerals and materials. *Rev. Mineral Geochem.* **71**, 271 (2010).

6. M. A. C. Wevers, J. C. Schon, M. Jansen, Determination of structure candidates of simple crystalline AB_2 systems. *J. Solid State Chem.* **136**, 233 (1998).

7. S. M. Woodley, P. D. Battle, J. D. Gale, C. R. A. Catlow, The prediction of inorganic crystal structures using a genetic algorithm and energy minimisation. *Phys. Chem. Chem. Phys.* **1**, 2535 (1999).

8. O. Delgado-Friedrichs, A. W. M. Dress, D. H. Huson, J. Klinowski, A. L. Mackay, Systematic enumeration of crystalline networks. *Nature* **400**, 644 (1999).

9. A. Le Bail, Inorganic structure prediction with GRINSP. *J. Appl. Crystallogr.* **38**, 389 (2005).

10. C. C. Fischer, K. J. Tibbetts, D. Morgan, G. Ceder, Predicting crystal structure by merging data mining with quantum mechanics. *Nature Mater.* **5**, 641 (2006).

11. O. Levy, G. L. W. Hart, S. Curtarolo, Uncovering compounds by synergy of cluster expansion and high-throughput methods. *J. Am. Chem. Soc.* **132**, 4830 (2010).

12. C. Mellot-Draznieks, J. M. Newsam, A. M. Gorman, C. M. Freeman, G. Ferey, De novo prediction of inorganic structures developed through automated assembly of secondary building units (AASBU method). *Angew. Chem. Int. Ed.* **39**, 2270 (2000).

13. X. Zhang, V. Stevanović, M. d'Avezac, S. Lany, A. Zunger, Prediction of A_2BX_4 metal-chalcogenide compounds via first-principles. *Phys. Rev. B* **86**, 014109 (2012).

14. P. Piquini, P. A. Graf, A. Zunger, Band-gap design of quaternary (In,Ga)(As,Sb) semiconductors via the inverse-band-structure approach. *Phys. Rev. Lett.* **100**, 186403 (2008).

15. J. Lima-de-Faria, E. Hellner, F. Liebau, E. Makovicky, E. Parthe, Nomenclature of inorganic structure types. Report of the International Union of Crystallography Commission on crystallographic nomenclature subcommittee on the nomenclature of inorganic structure types. *Acta Crystallogr.* **A46**, 1 (1990).

16. J. B. Thompson, Biopyriboles and polysomatic series. *Am. Mineral.* **63**, 239 (1978).

17. E. I. Gladishevskii, I. I. Zalutskii, G. T. Tivanchuk, Symmetry of superstructures in the series gold-copper-titanium-aluminum (AuCu3-TiAl3). *Visn. L'viv. Univ., Ser. Khim.* **14**, 9 (1972).

18. G. A. Jeffrey, V. Wu, The structure of the aluminum carbonitrides. II. *Acta Crystallogr.* **20**, 538 (1966).

19. G. Ferraris, E. Makovicky, S. Merlino, *Crystallography of modular materials*. (Oxford University Press, Oxford, 2004).

20. B. B. Zvyagin, S. Merlino, The pyroxene-spinel polysomatic system. *Z. Kristall.* **218**, 210 (2003).

21. R. H. Mitchell, *Perovskites: Ancient and modern*. (Almaz Press, Thunder Bay, Canada, 2002).

22. J. Darriet, M. A. Subramanian, Structural relationships between compounds based on the stacking of mixed layers related to hexagonal perovskite-type structures. *J. Mater. Chem.* **5**, 543 (1995).

23. I. Orlov, L. Palatinus, A. Arakcheeva, G. Chapuis, Hexagonal ferrites: a unified model of the $(TS)_nT$ series in superspace. *Acta Crystallogr.* **B63**, 703 (2007).

24. Ü. Özgür, Y. Alivov, H. Morkoç, Microwave ferrites, Part 1: Fundamental properties. *J. Mater. Sci.: Mater. Electron.* **20**, 789 (2009)

25. *Materials and methods are available as supplementary material on Science Online.*

26. A. Demont *et al.*, Stabilization of a complex perovskite superstructure under ambient conditions: Influence of cation composition and ordering, and evaluation as an SOFC cathode. *Chem. Mater.* **22**, 6598 (2010).

27. P. D. Battle, T. C. Gibb, P. Lightfoot, The crystal and magnetic-structures of $Sr_2LaFe_3O_8$. *J. Solid State Chem.* **84**, 237 (1990).

28. M. O. Zacate, R. W. Grimes, Combined Monte Carlo-energy minimization analysis of Al-Fe disorder in Ca_2FeAlO_5 brownmillerite. *Philos. Mag. A* **80**, 797 (2000).

29. S. Svarcová, K. Wiik, J. Tolchard, H. J. M. Bouwmeester, T. Grande, Structural instability of cubic perovskite $Ba_xSr_{1-x}Co_{1-y}Fe_yO_{3-d}$. *Solid State Ionics* **178**, 1787 (2008).

30. K. Wang, R. Ran, W. Zhou, H. Gu, Z. Shao, J. Ahn, Properties and performance of $Ba_{0.5}Sr_{0.5}Co_{0.8}Fe_{0.2}O_{3-d}$ + $Sm_{0.2}Ce_{0.8}O_{1.9}$ composite cathode. *J. Power Sources* **179**, 60 (2008).

31. V. Dusastre, J. A. Kilner, Optimisation of composite cathodes for intermediate temperature SOFC applications. *Solid State Ionics* **126**, 163 (1999).

32. J. Smit, H. P. J. Wijn, Eds., *Ferrites* (Wiley, New York and Eindhoven, 1959)

33. J. D. Gale, A. L. Rohl, The General Utility Lattice Program (GULP). *Mol. Simul.* **29**, 291 (2003).

34. B. G. Dick, A. W. Overhauser, Theory of the dielectric constants of alkali halide crystals. *Phys. Rev.* **112**, 90 (1958).

35. M. S. D. Read, M. S. Islam, G. W. Watson, F. King, F. E. Hancock, Defect chemistry and surface properties of $LaCoO_3$. *J. Mater. Chem.* **10**, 2298 (2000).

36. R. C. Baetzold, Atomistic simulation of ionic and electronic defects in $YBa_2Cu_3O_7$. *Phys. Rev. B* **38**, 11304 (1988).

37. T. S. Bush, J. D. Gale, C. R. A. Catlow, P. D. Battle, Self-consistent interatomic potentials for the simulation of binary and ternary oxides. *J. Mater. Chem.* **4**, 831 (1994).

38. C. A. J. Fisher, M. S. Islam, Mixed ionic/electronic conductors $Sr_2Fe_2O_5$ and $Sr_4Fe_6O_{13}$: atomic-scale studies of defects and ion migration. *J. Mater. Chem.* **15**, 3200 (2005).

39. A. Jones, M. S. Islam, Atomic-scale insight into $LaFeO_3$ perovskite: Defect nanoclusters and ion migration. *J. Phys. Chem. C* **112**, 4455 (2008).

40. G. Kresse, J. Furthmuller, Efficient iterative schemes for ab initio total-energy calculations using a plane-wave basis set. *Phys. Rev. B* **54**, 11169 (1996).

41. J. P. Perdew, K. Burke, M. Ernzerhof, Generalized gradient approximation made simple. *Phys. Rev. Lett.* **77**, 3865 (1996).

42. G. Kresse, D. Joubert, From ultrasoft pseudopotentials to the projector augmented-wave method. *Phys. Rev. B* **59**, 1758 (1999).

43. S. L. Dudarev, G. A. Botton, S. Y. Savrasov, C. J. Humphreys, A. P. Sutton, Electron-energy-loss spectra and the structural stability of nickel oxide: An LSDA+U study. *Phys. Rev. B* **57**, 1505 (1998).

44. L. Wang, T. Maxisch, G. Ceder, Oxidation energies of transition metal oxides within the GGA+U framework. *Phys. Rev. B* **73**, 195107 (2006).

45. Y.-L. Lee, J. Kleis, J. Rossmeisl, D. Morgan, Ab initio energetics of LaBO(3)(001) (B=Mn, Fe, Co, and Ni) for solid oxide fuel cell cathodes. *Phys. Rev. B* **80**, 224101 (2009).

46. A. C. Larson, R. B. Von Dreele, General Structure Analysis System (GSAS). *Los Alamos National Laboratory Report LAUR 86–748*, (2000).

47. H. T. Stokes, D. M. Hatch, B. J. Campbell. (2007).

48. K. Momma, F. Izumi, VESTA: a three-dimensional visualization system for electronic and structural analysis. *J. Appl. Crystallogr.* **41**, 653 (2008).
49. A. M. Kevorkov *et al.*, Y_2O_3 Single-crystals - growth, structure, and photoinduced effects. *Kristallografiya* **40**, 28 (1995).
50. P. W. Stephens, Phenomenological model of anisotropic peak broadening in powder diffraction. *J. Appl. Crystallogr.* **32**, 281 (1999).
51. A. S. Wills, A new protocol for the determination of magnetic structures using simulated annealing and representational analysis (SARAh). *Phys. B* **276**, 680 (2000).
52. C. T. Koch, thesis, Arizona State University (2002).
53. N. L. Allan, G. D. Barrera, M. Y. Lavrentiev, I. T. Todorov, J. A. Purton, Ab initio calculation of phase diagrams of ceramics and minerals. *J. Mater. Chem.* **11**, 63 (2001).

Fig. 1:A) A modular description of the aluminium carbonitride structural family. Modules of composition Al_2C (blue), AlC (red) and AlN (orange) are used to describe the extended structures of $Al_6C_3N_2$ and $Al_8C_3N_4$(*23*). B) A modular description of the hexaferrite structural family. Modules of composition $Ba_2Fe_8O_{14}$ (T-block, blue), $(BaFe_6O_{11})^{2-}$ (R-block, red) and $(Fe_6O_8)^{2+}$ (S-block, orange) are used to describe the extended structures of W-type and Z-type hexaferrites (*32*). C) A schematic outlining the EMMA method of constructing and screening possible structures arising from extended modular units. In this case, four layered units are chosen, with two equivalent units. All twelve permutations of these units are built into structures, of which three are unique under translational symmetry. These three are tested, and the best structure chosen.
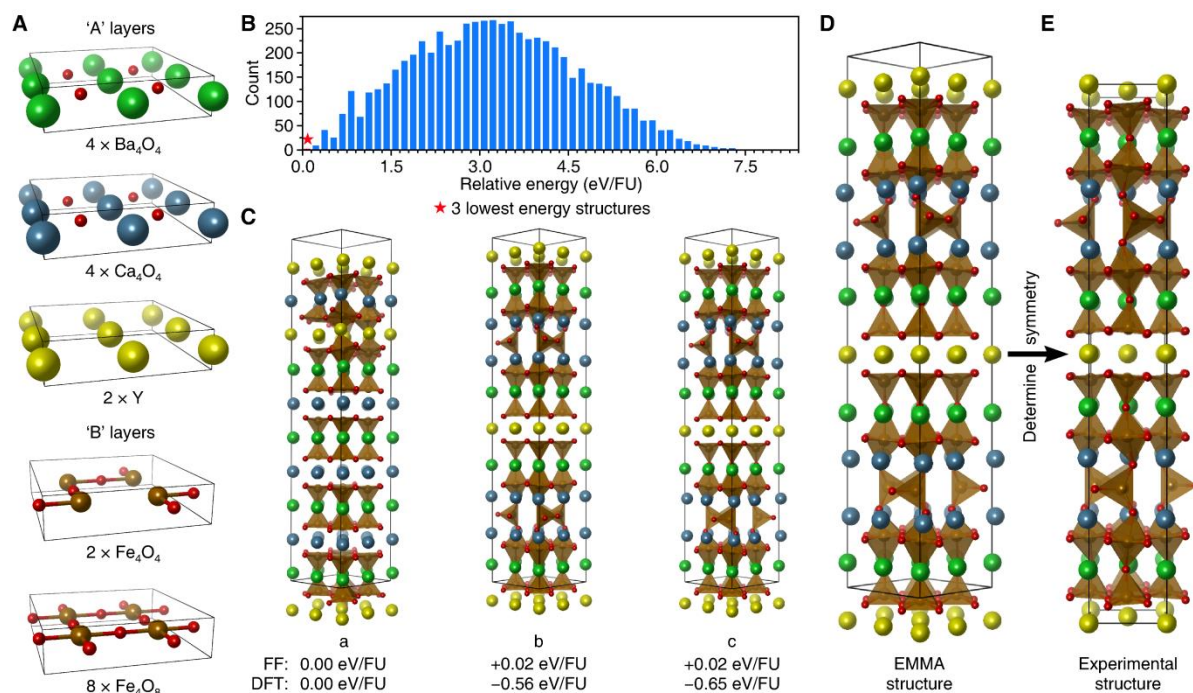
Fig. 2: The $10a_p$ Structure of $YBa_2Ca_2Fe_5O_{13}$. A) The A- and B- site layered units used as the base structural modules throughout this work, B) a graph showing the force-field energies of all calculated structures, C) the three lowest energy structures predicted from force-field calculations and their relative energies calculated using both force-fields and DFT, D) the lowest energy structure from EMMA and E) the refined experimental structure. Atoms are colored as follows: Yellow Y, green Ba, blue Ca, brown Fe and red O.
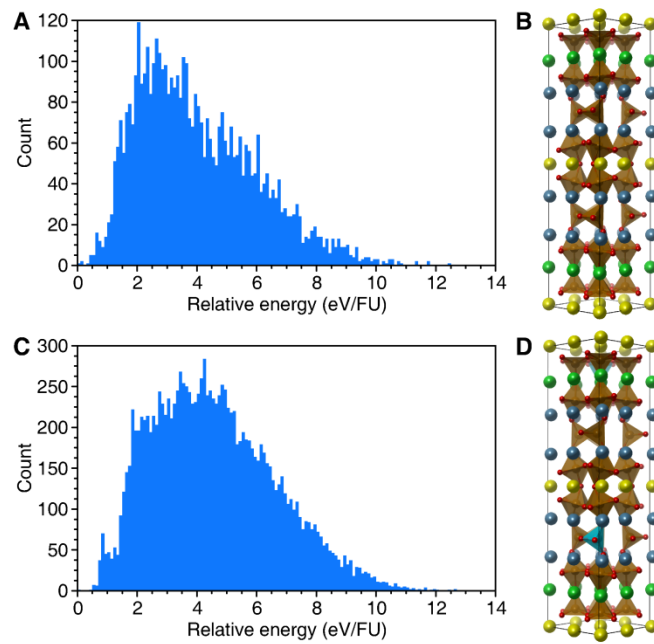
Fig. 3: EMMA calculations on structures with an $8a_p$ repeat. The energies of structures with the composition $Y_2Ba_2Ca_4Fe_8O_{21}$ with converged force-field calculations are plotted in A, and those with composition $Y_2Ba_2Ca_4Fe_{7.5}Cu_{0.5}O_{21}$ are plotted in C. The most stable $Y_2Ba_2Ca_4Fe_8O_{21}$ and $Y_2Ba_2Ca_4Fe_{7.5}Cu_{0.5}O_{21}$ structures are shown in B and D respectively. Atoms are colored as follows: Yellow Y, green Ba, blue Ca, brown Fe, light blue Cu and red O.
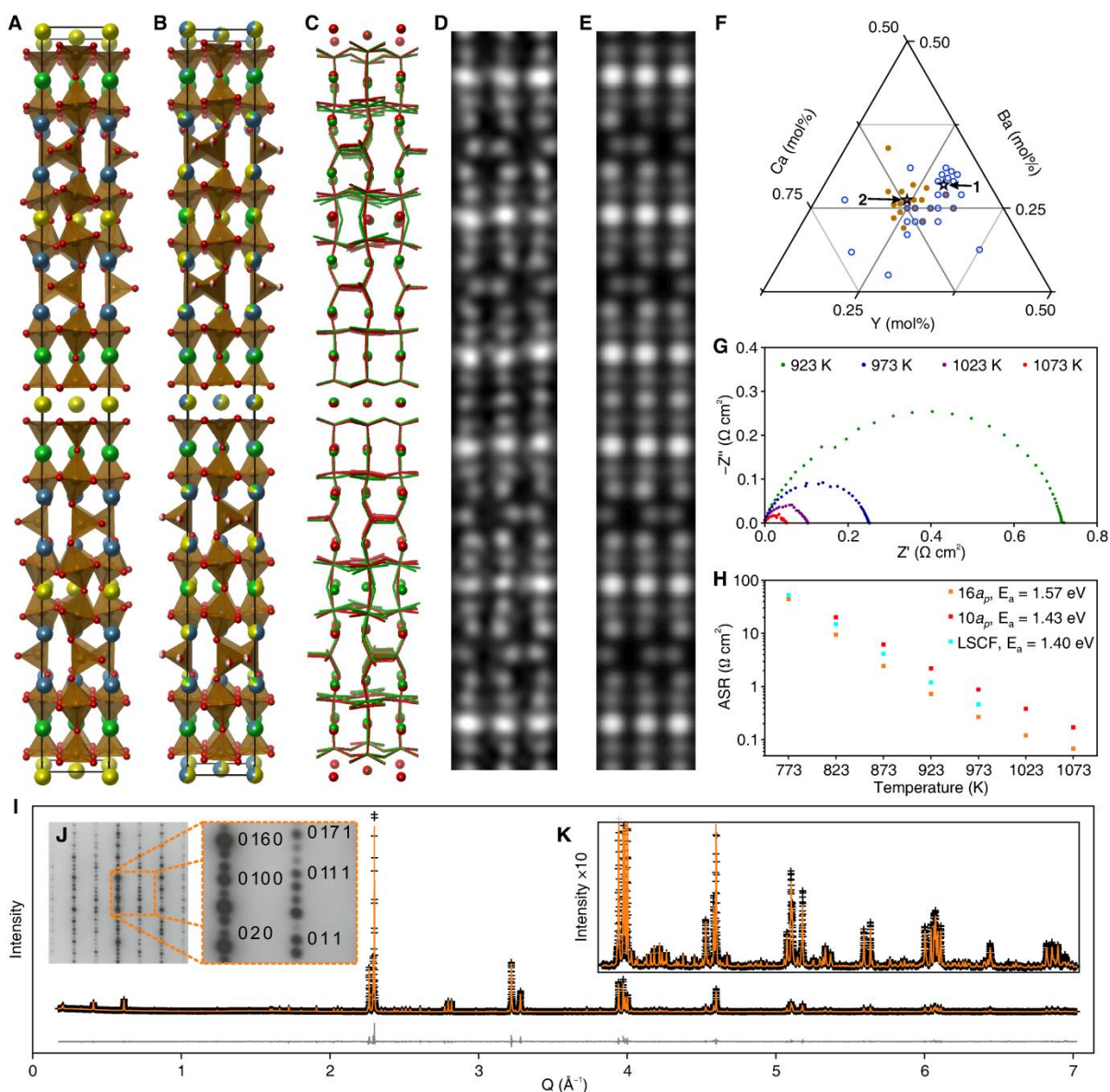
Fig. 4: The $16a_p$ Structure. A) The $16a_p$ structure as predicted by EMMA is compared with

B) the refined structure of **1**. Atoms are colored as follows: Yellow Y, green Ba, blue Ca,

brown Fe/Cu and red O. C) Overlaid EMMA (green) and refined experimental (red)

structures. D) Observed and E) calculated HAADF-STEM images of the $16a_p$ phase. F)

Compositional phase diagram showing the compositions investigated to isolate **1** (open blue

circles) and **2** (closed brown circles). The compositions of **1** and **2** are highlighted with a star.

G) A Z-Z* plot showing cathode performance of **1** in a symmetrical cell on a GDC

electrolyte at temperatures between 923 and 1073 K. H) Area specific resistance (ASR)

values obtained at temperatures between 773 K and 1073 K for **1** compared to literature

values reported for $10a_p$ (*26*) and LSCF (*31*). I) Refined X-ray diffraction data (*25*) showing observed (black crosses), calculated (orange line) and difference (grey line) data. Tabulated crystallographic data can be found in Table S1 and refined neutron powder diffraction data in Fig. S13. An electron diffraction pattern of **1** showing the $16a_p$ repeat (J) and an enlarged high Q region of the diffraction data (K) are shown inset.

Supplementary Materials:

www.sciencemag.org

Materials and Methods

Supplementary Text

Figs. S1, S2, S3, S4, S5, S6, S7, S8, S9, S10, S11, S12, S13

Table S1

References (*33-53*) [Note: The numbers refer to any additional references cited only within the Supplementary Materials]